

Article

Shell Model Description of Spin-Dependent Elastic and Inelastic WIMP Scattering off ^{119}Sn and ^{121}Sb

Joona Kasurinen ^{1,*}, Jouni Suhonen ¹ , Praveen C. Srivastava ² and Pekka Pirinen ¹

¹ Department of Physics, University of Jyväskylä, P.O. Box 35 (YFL), 40014 Jyväskylä, Finland; jouni.t.suhonen@jyu.fi (J.S.); pekka.a.pirinen@jyu.fi (P.P.)

² Department of Physics, Indian Institute of Technology Roorkee, Roorkee 247667, India; praveen.srivastava@ph.iitr.ac.in

* Correspondence: joona.m.kasurinen@jyu.fi

Abstract: In this work, we calculate the spin structure functions for spin-dependent elastic and inelastic WIMP scattering off ^{119}Sn and ^{121}Sb . Estimates for detection rates are also given. ^{119}Sn and ^{121}Sb are amenable to nuclear structure calculations using the nuclear shell model (NSM). With the possible exception of ^{201}Hg , they are the only such nuclei still unexplored theoretically for their potential of inelastic WIMP scattering to a very low excited state. The present calculations were conducted using a state-of-the-art WIMP–nucleus scattering formalism, and the available effective NSM two-body interactions describe the spectroscopic properties of these nuclei reasonably well. Structure functions were found to be high for both nuclei in the case of elastic scattering. Elastic scattering dominated at the zero momentum transfer limit. Detection rate calculations indicated that inelastic scattering was relevant for both nuclei, even surpassing elastic rates for some recoil energies.

Keywords: dark matter; WIMP; direct detection; spin structure functions; nuclear structure



Citation: Kasurinen, J.; Suhonen, J.; Srivastava, P.C.; Pirinen, P. Shell Model Description of Spin-Dependent Elastic and Inelastic WIMP Scattering off ^{119}Sn and ^{121}Sb . *Universe* **2022**, *8*, 309. <https://doi.org/10.3390/universe8060309>

Academic Editor: Csaba Balazs

Received: 19 April 2022

Accepted: 29 May 2022

Published: 31 May 2022

Publisher's Note: MDPI stays neutral with regard to jurisdictional claims in published maps and institutional affiliations.



Copyright: © 2022 by the authors. Licensee MDPI, Basel, Switzerland. This article is an open access article distributed under the terms and conditions of the Creative Commons Attribution (CC BY) license (<https://creativecommons.org/licenses/by/4.0/>).

1. Introduction

Galaxy rotation curves [1–4] and structure formation [5,6] indicate that either our present understanding of gravity is wrong or most of the matter in the universe is comprised of a dark component of unknown nature. Recent experiments [7,8] analyzing the cosmic microwave background (CMB) have given yet more credibility to standard cosmology in which there is around five times as much dark matter as there is regular matter. Competing theories do exist, such as modified Newtonian dynamics (MOND) [9] and Tensor-Vector-Scalar (TeVeS) gravity [10], f(R) gravity [11], as well as dark fluid [12] and negative mass [13], to name a few. Challenges to modified gravity theories are posed by weak lensing studies [14,15] and gravitational wave measurements [16]. Nevertheless, some of them are left standing, and the debate continues.

Assuming dark matter is explained by some kind of undiscovered particles, the particles would likely be nonrelativistic and rather massive. This is the standard dark matter picture, where non-baryonic weakly interacting massive particles (WIMPs) are introduced. The theoretical motivation for WIMPs can be found in several frameworks ranging from Kaluza–Klein theories [17,18] to technicolor [19,20], little Higgs [21,22], and supersymmetry [23]. To detect these massive WIMPs, a direct way would be to observe their scattering from atomic nuclei. Hence, nuclei would be an excellent direct probe of the properties of dark matter [24]; therefore the search for good candidate nuclei is of paramount importance.

The mechanism of the WIMP–nucleus interaction is unknown, so that ideal detectors would consist of nuclei that are sensitive to both coherent and incoherent interactions and also allow inelastic scattering of WIMPs. Unfortunately, such a combination of properties excludes almost all nuclei available for experiments. However, should one want to study

both incoherent elastic and inelastic scattering off nuclei, the ideal target would be an odd-proton or odd-neutron nucleus, offering low-energy excited states and allowing spin-dependent scattering off nuclei. Such possible targets have been identified for some iodine, xenon, and cesium nuclei [25–28]. Beyond these, the nuclei ^{83}Kr and ^{125}Te , with a very low-energy first excited state, were studied in [29–31]. These studies have been conducted by exploiting the nuclear wave functions obtained by the use of the nuclear shell model (NSM). In [32], the microscopic interacting boson–fermion model (IBFM-2) was used for the first time to discuss spin-dependent WIMP–nucleus scattering off ^{125}Te , ^{129}Xe , and ^{131}Xe . The results were benchmarked against the earlier NSM results of [27,28,33]. In these studies, the one-body and leading long-range two-body WIMP–nucleus currents derived from the chiral effective field theory (c-EFT) [27] were employed.

Very recently in [34], the IBFM-2 was applied to describe the elastic and inelastic WIMP scattering cross sections off ^{183}W . This was the first time that the scattering of WIMPs off a heavy deformed nucleus was described successfully. The used scattering formalism was updated by adopting the formalism of [35], where the contributions from all pion-exchange, pion-pole, and contact currents were taken into account. We use this same scattering formalism in the present work but compute the nuclear wave functions of the ground and first excited states of ^{119}Sn and ^{121}Sb by using the NSM. In these nuclei, the excitation energy of the first excited state ($3/2^+$ state at 23.87 keV in ^{119}Sn and $7/2^+$ state at 37.13 keV in ^{121}Sb) is very low; thus, these nuclei are good candidates for direct detection of dark matter by inelastic scattering, where the background signal can be reduced by exploiting coincidence with the involved magnetic dipole (M1) transition to the ground state.

For observation of inelastic WIMP–nucleus scattering, the target nuclei should have a low excited state below some 100 keV. These nuclei are heavy or very heavy and often deformed. To our knowledge, there are only three nuclei still unexplored for spin-dependent WIMP scattering to a low excited state that are at the same time suitable for NSM description owing to their (near) semi-magicity. Two of them are the presently discussed ^{119}Sn and ^{121}Sb . The third is ^{201}Hg , which is very heavy and hard to describe with adequate precision using presently available shell-model interactions.

2. Cross Section and Spin Structure

There are many factors that influence the probability of WIMP–nucleus scattering. After stripping off extrinsic factors such as dark matter density and the size of the detector, we are left with the scattering cross section. Going deeper, we can take out more factors until what is left is just the nuclear physics. This is the idea of the spin structure functions.

The cross section of spin-dependent WIMP–nucleus scattering can be derived from effective field theory (EFT). It is related to the structure functions by the following Equation [36]:

$$\frac{d\sigma}{dq^2} = \frac{8G_F^2}{(2J+1)v^2} S_A(q), \quad (1)$$

where G_F is the Fermi coupling constant, J is the ground state angular momentum, and v is the speed of the WIMP in the laboratory frame. S_A is the axial structure function, which contains the nuclear physics. It is a function of momentum transfer q . Knowing the structure functions of a nucleus means knowing how the nuclear structure contributes to the scattering cross section.

The structure functions were determined following the formalism of [27,35], in which two-body currents are included as effective one-body currents via a normal-ordering approximation. The values chosen for the low-energy couplings and nuclear density were $c_1 = -1.20(17) \text{ GeV}^{-1}$, $c_3 = -4.45(86) \text{ GeV}^{-1}$, $c_4 = 2.69(70) \text{ GeV}^{-1}$, $\hat{c}_6 = 5.83$, $c_D = -8.0 \dots 2.0$, and $\rho = 0.11(1) \text{ fm}^{-3}$. See Table 1 for a summary. The parameter choices were based on [34,35,37]. For \hat{c}_6 , having a range of values is not necessary, because the results are insensitive to it. As for the others, we calculated the smallest and largest theoretically possible values for the structure functions given these ranges of parameters. The calculation was performed for each of the four cases: elastic scattering off ^{119}Sn , inelastic scattering off ^{119}Sn ,

elastic scattering off ^{121}Sb , and inelastic scattering off ^{121}Sb . In addition, the same calculations were performed a second time using one-body currents only.

Table 1. Parameters fed into the WIMP scattering program.

Param.	Values
c_1	$-1.37 \dots -1.03 \text{ GeV}^{-1}$
c_3	$-5.31 \dots -3.59 \text{ GeV}^{-1}$
c_4	$1.99 \dots 3.39 \text{ GeV}^{-1}$
\hat{c}_6	5.83
c_D	$-8.0 \dots 2.0$
ρ	$0.10 \dots 0.12 \text{ fm}^{-3}$

3. Shell Model Calculations

The nuclear structure is entered into the WIMP scattering program in the form of one-body transition densities (OBTD). These were obtained by a shell model calculation. The calculations were performed in the 50–82 model space with the realistic CD-Bonn interaction [38].

The CD-Bonn potential based on meson exchange is the charge-dependent one-boson-exchange nucleon–nucleon potential fitted for proton–proton data below 350 MeV. The reproduction of data is more accurate than with phase-shift analysis or other nucleon–nucleon potentials. The charge dependence of the present potential is based on the predictions by the Bonn full model for charge symmetry and charge-independence breaking. The nonlocality of the potential is represented in terms of the covariant Feynman amplitudes for one-boson exchange. The interaction was renormalized using the perturbative G-matrix approach [39]. The renormalization effectively takes into account the single-particle space outside the presently used valence space. The effective single-particle energies were taken as 0.0 ($0g_{7/2}$), 0.172 ($1d_{5/2}$), 2.55 ($1d_{3/2}$), 2.45 ($2s_{1/2}$), and 3.00 ($0h_{11/2}$) MeV, respectively. These effective energies can be viewed as phenomenological renormalization coming from our restricted valence space and three-body forces neglected in the bare shell-model Hamiltonian. Earlier shell model results with this interaction are reported in Refs. [40,41]. The shell model calculations were carried out using the codes NuShellX [42] and KShell [43].

The shell model calculation gave reasonable predictions for the lowest two states (see Figure 1). The most notable deviation from the experiment is that the first two states of ^{121}Sb were flipped. In addition, the energies were not replicated exactly. However, what is more relevant is that the magnetic dipole moments and electric quadrupole moments were correct, because this indicates that the wave functions contained the components that captured the nuclear spectroscopy relevant for WIMP–nucleus scattering.

In Table 2, we have reported the leading configurations of the two lowest states of ^{119}Sn and ^{121}Sb . For ^{119}Sn , only the neutrons were active, and the wave functions of the lowest $1/2^+$ and $3/2^+$ states were quite fragmented with the leading components having the $1d_{5/2}$ orbital filled and the $0g_{7/2}$ orbital either filled or having two holes. The higher orbitals had varying degrees of occupation. In the case of the lowest $5/2^+$ and $7/2^+$ states in ^{121}Sb , the fragmentation was again strong with the neutron side possessing features similar to that of ^{119}Sn . On the proton side, the $5/2^+$ state was described as a proton in the $1d_{5/2}$ orbital, and the $7/2^+$ state was characterized as a proton in the $0g_{7/2}$ orbital.

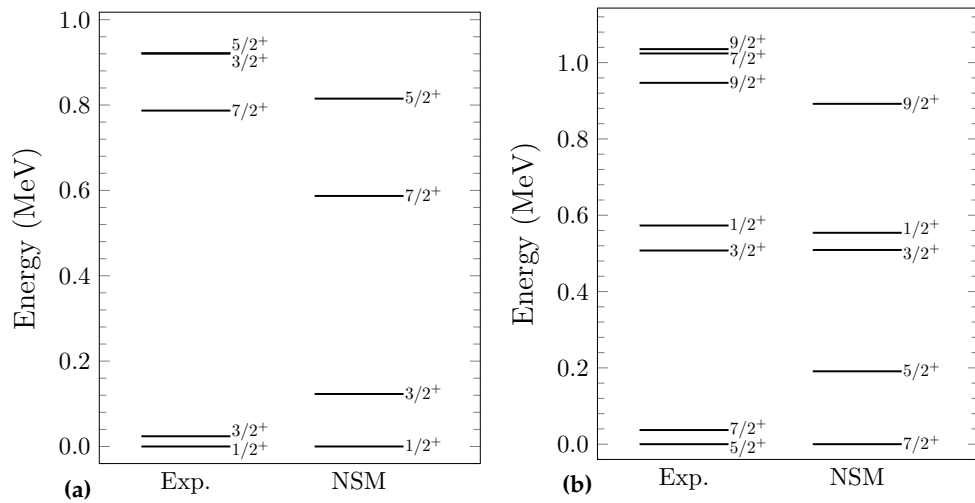


Figure 1. Comparison of experimental and calculated states: (a) left panel is for ^{119}Sn , with experimental values from Ref. [44], and (b) right panel is for ^{121}Sb , with experimental values from Ref. [45]. Ground state and first excited state are flipped for ^{121}Sb .

Table 2. The configurations of the lowest-lying states of ^{119}Sn and ^{121}Sb .

Nucleus	J^π	Configuration
^{119}Sn	$1/2^+$	$\nu(g_{7/2}^6 d_{5/2}^6 d_{3/2}^2 s_{1/2}^1 h_{11/2}^4)$ (17.5%) $\nu(g_{7/2}^8 d_{5/2}^6 d_{3/2}^0 s_{1/2}^1 h_{11/2}^4)$ (14.4%) $\nu(g_{7/2}^6 d_{5/2}^6 d_{3/2}^0 s_{1/2}^1 h_{11/2}^6)$ (10.9%) $\nu(g_{7/2}^8 d_{5/2}^6 d_{3/2}^2 s_{1/2}^1 h_{11/2}^2)$ (5.5%)
	$3/2^+$	$\nu(g_{7/2}^8 d_{5/2}^6 d_{3/2}^1 s_{1/2}^0 h_{11/2}^4)$ (12.8%) $\nu(g_{7/2}^6 d_{5/2}^6 d_{3/2}^1 s_{1/2}^2 h_{11/2}^4)$ (11.8%) $\nu(g_{7/2}^6 d_{5/2}^6 d_{3/2}^1 s_{1/2}^0 h_{11/2}^6)$ (10.9%) $\nu(g_{7/2}^6 d_{5/2}^6 d_{3/2}^3 s_{1/2}^1 h_{11/2}^4)$ (6.6%) $\nu(g_{7/2}^8 d_{5/2}^6 d_{3/2}^1 s_{1/2}^2 h_{11/2}^2)$ (5.4%)
^{121}Sb	$5/2^+$	$\pi(d_{5/2}^1) \otimes \nu(g_{7/2}^6 d_{5/2}^6 d_{3/2}^2 s_{1/2}^0 h_{11/2}^6)$ (8.6%) $\pi(d_{5/2}^1) \otimes \nu(g_{7/2}^6 d_{5/2}^6 d_{3/2}^2 s_{1/2}^1 h_{11/2}^4)$ (6.9%) $\pi(d_{5/2}^1) \otimes \nu(g_{7/2}^8 d_{5/2}^6 d_{3/2}^2 s_{1/2}^0 h_{11/2}^4)$ (4.6%)
	$7/2^+$	$\pi(g_{7/2}^1) \otimes \nu(g_{7/2}^6 d_{5/2}^6 d_{3/2}^2 s_{1/2}^0 h_{11/2}^6)$ (9.6%) $\pi(g_{7/2}^1) \otimes \nu(g_{7/2}^6 d_{5/2}^6 d_{3/2}^2 s_{1/2}^1 h_{11/2}^4)$ (4.7%) $\pi(g_{7/2}^1) \otimes \nu(g_{7/2}^6 d_{5/2}^6 d_{3/2}^0 s_{1/2}^1 h_{11/2}^6)$ (4.4%)

The shell model calculation produced reasonable nuclear moments. A summary of the calculated and experimental moments is presented in Table 3.

For ^{119}Sn , the experimental values for the magnetic moments in the ground state and first excited state were $-1.0459(5)\mu_N$ and $+0.633(3)\mu_N$, respectively, [44]. These were close to the calculated values $-1.213\mu_N$ and $+0.749\mu_N$. The quadrupole moment of the first excited state was $-0.132(1)$ eb, which in our calculations was -0.107 eb. Based on these comparisons, the shell model calculation produces wave functions that are reasonably realistic for the purposes of our WIMP calculation.

For ^{121}Sb , the magnetic moments were $+3.3580(16)\mu_N$ in the ground state and $+2.518(7)\mu_N$ in the first excited state [45]. According to our shell model calculation, these values were $+3.681\mu_N$ and $+1.185\mu_N$. The values are reasonable, though the second one was not as accurate. Quadrupole moments for the ground state and first excited state were experimentally $-0.543(11)$ eb and $-0.727(16)$ eb, and according to our shell model calculation, they were -0.439 eb and -0.559 eb, in reasonable agreement with the data.

Table 3. Comparison between calculated and experimental nuclear moments in the lowest two states of ^{119}Sn and ^{121}Sb . Effective charges and g-factors were $e_p = 1.5e$, $e_n = 0.5e$, $g_l^{eff} = g_l^{free}$, and $g_s^{eff} = g_s^{free}$.

State	$\mu (\mu_N)$ exp.	$\mu (\mu_N)$ NSM	Q (eb) exp.	Q (eb) NSM
$^{119}\text{Sn } 1/2^+$	−1.0459(5)	−1.213	-	-
$^{119}\text{Sn } 3/2^+$	+0.633(3)	+0.749	−0.132(1)	−0.107
$^{121}\text{Sb } 5/2^+$	+3.3580(16)	+3.681	−0.543(11)	−0.439
$^{121}\text{Sb } 7/2^+$	+2.518(7)	+1.185	−0.727(16)	−0.559

It is also of interest to examine how well the computed wave functions described the electromagnetic transitions between the lowest few states. In Table 4, a comparison of the calculated and available experimental electric quadrupole (E2) and magnetic dipole (M1) transitions is shown. For ^{119}Sn the reduced E2 transition probabilities, $B(E2)$, were in reasonable agreement with the data. Notably, the experimental reduced M1 transition probability, $B(M1)$, was quite well reproduced by the calculations. This is relevant for the inelastic WIMP scattering to the $3/2^+$ state, since this scattering was mainly of the M1 type, mediated by the Pauli spin operator σ at the zero momentum exchange limit. The contrary was true for ^{121}Sb for which the computed $B(M1)$ was roughly an order of magnitude too low; thus, the cross section of inelastic scattering to the $7/2^+$ state was likely underestimated.

Table 4. Reduced transition probabilities and energies for electromagnetic transitions between the lowest few states in ^{119}Sn and ^{121}Sb . The effective charges and g-factors used were $e_p = 1.5e$, $e_n = 0.5e$, $g_l^{eff} = g_l^{free}$, and $g_s^{eff} = g_s^{free}$.

Nuc.	Transition	B (W.u.) exp.	B (W.u.) NSM	E_γ (keV) exp.	E_γ (keV) NSM
^{119}Sn	E2: $\frac{3}{2}^+ \rightarrow \frac{1}{2}^+$	<0.70	0.40	23.870(8)	123
	E2: $\frac{5}{2}^+ \rightarrow \frac{1}{2}^+$	5(3)	1.99	921.4(2)	815
	E2: $\frac{5}{2}^+ \rightarrow \frac{3}{2}^+$	17(6)	2.75	897.5(2)	693
	M1: $\frac{3}{2}^+ \rightarrow \frac{1}{2}^+$	0.015	0.017	23.870(8)	123
^{121}Sb	M1: $\frac{7}{2}^+ \rightarrow \frac{5}{2}^+$	0.01047(17)	0.00072	37.1298(2)	191

4. WIMP Scattering Results

We express the structure functions in terms of recoil energy $E_R = q^2/2m_A = u/b^2m_A$, where u is a dimensionless variable, b is the harmonic oscillator length, q is the momentum transfer, and m_A is the mass of the nucleus. The harmonic oscillator length b is a parameter describing the range of the harmonic oscillator wave functions that were used as the basis in the shell model calculations [46].

We break down S_A by its isoscalar and isovector components as

$$S_A(u) = a_0^2 S_{00}(u) + a_0 a_1 S_{01}(u) + a_1^2 S_{11}(u), \tag{2}$$

and then express the results as “neutron-only” and “proton-only” couplings

$$S_n(u) = S_{00}(u) - S_{01}(u) + S_{11}(u), \quad S_p(u) = S_{00}(u) + S_{01}(u) + S_{11}(u). \tag{3}$$

The functions $S_{\rho\rho'}$ (u) are defined in [31]. This division to “neutron-only” and “proton-only” structure functions is conventionally used, but is not entirely accurate when two-body currents are included (see [27] for discussion).

The structure functions S_n and S_p for ^{119}Sn and ^{121}Sb are shown as functions of recoil energy E_R in Figures 2 and 3. The thickness of the S_n and S_p curves show the error resulting from the uncertainties in the EFT low-energy constants and nuclear density.

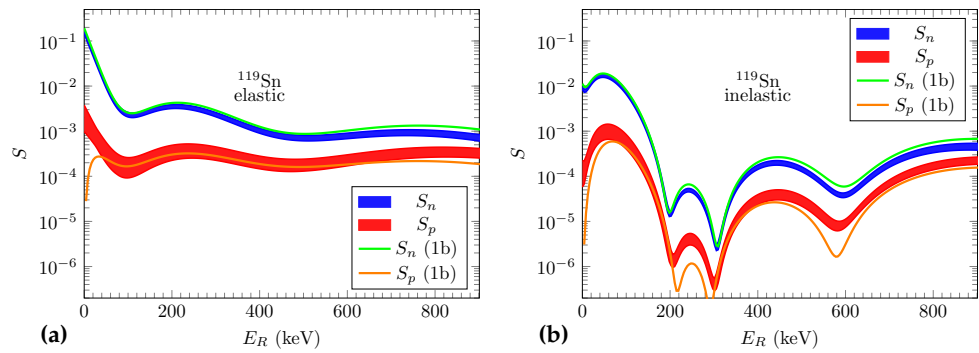


Figure 2. Structure functions of nucleus ^{119}Sn : (a) Left panel shows neutron-only and proton-only structure functions in the case of elastic scattering (nucleus remains in the ground state $1/2^+$). (b) Right panel shows neutron-only and proton-only structure functions in the case of inelastic scattering (nucleus excites to the first excited state $3/2^+$). $S_{n,p}(1b)$ are with one-body currents only.

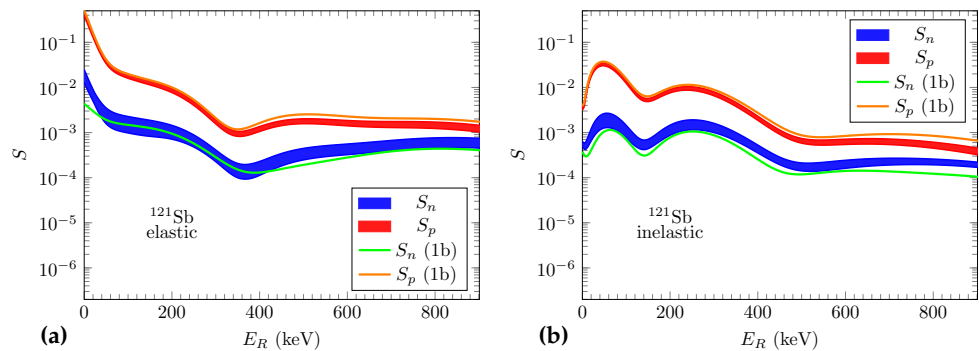


Figure 3. Structure functions of nucleus ^{121}Sb : (a) Left panel shows neutron-only and proton-only structure functions in the case of elastic scattering (nucleus remains in the ground state $5/2^+$). (b) Right panel shows neutron-only and proton-only structure functions in the case of inelastic scattering (nucleus excites to the first excited state $7/2^+$). $S_{n,p}(1b)$ are with one-body currents only.

The elastic scattering structure functions were high for both nuclei: ^{119}Sn was similar to ^{125}Te and ^{129}Xe [27,32,47], while for ^{121}Sb , the functions were higher still. For the inelastic scattering from ^{119}Sn , there was a large dip between $E_R = 100$ keV and $E_R = 700$ keV. For ^{121}Sb , on the other hand, the inelastic scattering structure functions were on par with the elastic ones starting at around $E_R = 50$ keV.

It could be safer to take the inelastic result for ^{121}Sb as a lower limit, since the calculated transition probability for the corresponding M1 transition was an order of magnitude smaller than the measured one. It can also be seen in the figures that for ^{121}Sb already the one-body contribution produced realistic structure functions, whereas for ^{119}Sn there were notable contributions by two-body currents to S_p in the elastic case for recoil energies below some 50 keV and in the inelastic case within several recoil energy intervals.

The spin expectation values of the ground state are important in elastic scattering. They determine the structure functions in the zero momentum transfer limit by the following equation:

$$S_A(0) = \frac{(2J+1)(J+1)}{4\pi J} \left| (a_0 + a_1 + \delta a_1(0)) \langle S_p \rangle + (a_0 - a_1 - \delta a_1(0)) \langle S_n \rangle \right|^2. \quad (4)$$

The spin expectation values for ^{119}Sn were found to be $\langle S_p \rangle = 0$ and $\langle S_n \rangle = 0.31712$. For ^{121}Sb , they were $\langle S_p \rangle = 0.43887$ and $\langle S_n \rangle = 0.04041$.

The differential event rates can be estimated for a given WIMP mass. This was calculated following [28,34]. The results of the event rate calculations are shown in Figures 4–6. It is assumed that coupling was only with the unpaired nucleon. This is justified by the

structure functions of the unpaired nucleon being about an order of magnitude higher than those of the paired nucleon.

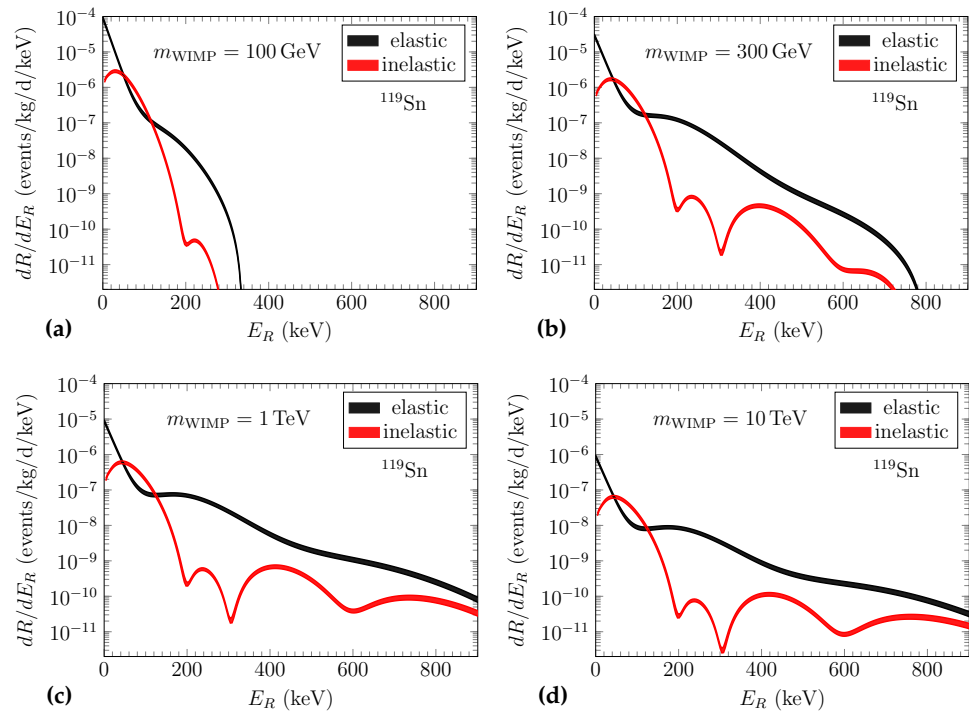


Figure 4. Differential event rates in ^{119}Sn with WIMP masses: (a) 100 GeV; (b) 300 GeV; (c) 1 TeV; and (d) 10 TeV.

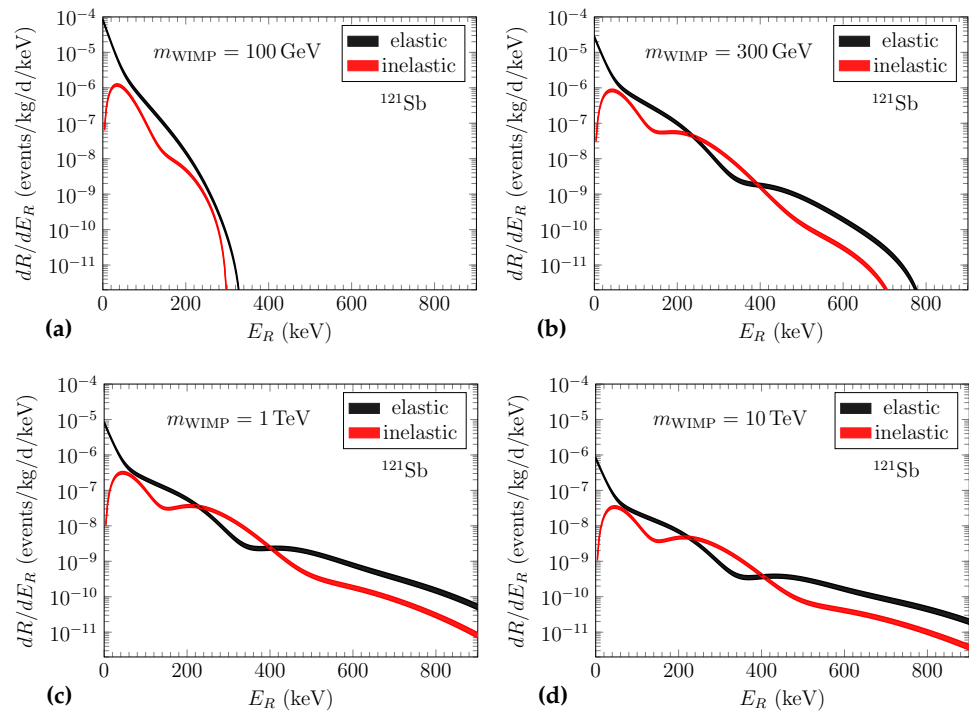


Figure 5. Differential event rates in ^{121}Sb with WIMP masses: (a) 100 GeV; (b) 300 GeV; (c) 1 TeV; and (d) 10 TeV.

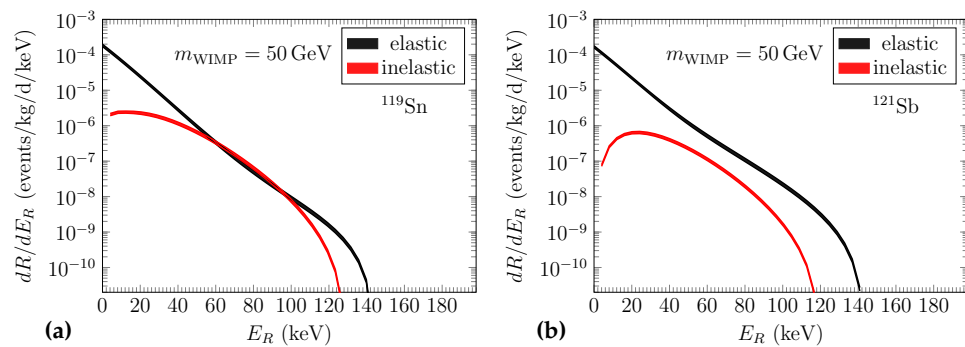


Figure 6. Differential event rates for WIMPs of mass 50 GeV: (a) in ^{119}Sn and (b) in ^{121}Sb .

For low mass WIMPs, event rates move quickly to zero for higher recoil energies. This is because WIMPs of a sufficiently low mass simply do not have enough momentum to make the much heavier nucleus recoil past a certain maximum recoil energy. The most dramatic change in the shape of the differential event rate graphs is seen when the WIMP mass passes the mass of the nucleus at around 120 GeV. For WIMP masses larger than this, the overall shape of the event rate curve stays the same, though the slope becomes steeper (when viewed through a linear scale). The event rate is close to inversely proportional to the WIMP mass in the low recoil energy region. This is most apparent when comparing the graphs for 1 TeV and 10 TeV WIMPs.

In terms of the event rate, both nuclei performed similarly in the case of elastic scattering. ^{119}Sn had higher differential event rates for inelastic scattering at the zero momentum transfer limit, because the rates did not fall so steeply when approaching zero. However, for inelastic scattering there was a large dip between 100 keV and 700 keV. For ^{121}Sb , the inelastic differential event rates were low for small recoil energies, climbed fast to a peak near 40 keV, and then remained within an order of magnitude of their elastic counterparts. For WIMPs near the low end of the possible mass range, inelastic scattering was about an order of magnitude more important in ^{119}Sn than in ^{121}Sb . See Figure 6 for the differential event rates of 50 GeV WIMPs. However, due to the previously mentioned underprediction of the M1 transition probability in ^{121}Sb , this conclusion may be incorrect. For masses nearing 10 GeV, elastic scattering was restricted to small recoil energies, and inelastic scattering becomes impossible.

5. Discussion

Our calculations showed that the structure functions corresponding to the unpaired nucleon were consistently about an order of magnitude larger: neutron-only structure functions were more important for ^{119}Sn , and proton-only structure functions were more important for ^{121}Sb . This is expected, as similar results are seen in the literature for various other nuclei.

When compared with other nuclei, the elastic scattering structure functions of ^{119}Sn were similar in shape and magnitude to those of ^{125}Te and ^{129}Xe [27,32,47]. The structure functions of ^{121}Sb were higher still, making ^{121}Sb a promising WIMP detector. In particular, the proton-only elastic scattering structure function of ^{121}Sb was about 0.4 near the zero momentum transfer limit. This is among the highest values seen in the literature.

The most noticeable difference between the two nuclei is that there was a large dip in the inelastic structure functions of ^{119}Sn . After reaching its maximum at around 50 keV, both the proton-only and neutron-only structure functions plummeted several orders of magnitude. This dip was also seen in the corresponding event rates. ^{121}Sb had no such dip, and so for ^{121}Sb , the event rates for inelastic scattering were comparable to those of elastic scattering across a wide range of recoil energies.

^{119}Sn had better inelastic event rates below 100 keV, while the elastic event rates in this zone were similar. Therefore, ^{119}Sn had a better overall event rate than ^{121}Sb in the sub 100 keV region. For low mass WIMPs, this is the only region that matters, in which case

^{119}Sn would be the better choice. If WIMPs are heavy, then the answer is not so simple. WIMPs heavier than the detector nuclei can result in a wider range of recoil energies. In this case, ^{121}Sb may be more suitable, though one must note that, in general, events with higher recoil energy are much less likely.

Author Contributions: WIMP–nucleus scattering calculations, writing of the paper, J.K.; NSM calculations, writing of the paper, P.C.S.; original idea about the nuclei to be discussed, writing of the paper, J.S.; updates and instruction of use of the WIMP–nucleus scattering programs, P.P. All authors have read and agreed to the published version of the manuscript.

Funding: This work was partially supported by the Academy of Finland under the Project No. 318043. P.C.S. acknowledges a research grant from SERB (India), CRG/2019/000556.

Institutional Review Board Statement: Not applicable.

Informed Consent Statement: Not applicable.

Conflicts of Interest: The authors declare no conflict of interest.

References

- Zwicky, F. Die rotverschiebung von extragalaktischen nebeln. *Helv. Phys. Acta* **1933**, *6*, 110.
- Rubin, V.C.; Ford, W.K., Jr. Rotation of the andromeda nebula from a spectroscopic survey of emission regions. *Astrophys. J.* **1970**, *159*, 379. [[CrossRef](#)]
- Einasto, J.; Kaasik, A.; Saar, E. Dynamic evidence of massive coronas of galaxies. *Nature* **1974**, *250*, 309. [[CrossRef](#)]
- Roberts, M.S.; Whitehurst, R.N. The rotation curve and geometry of M31 at large galactocentric distances. *Astrophys. J.* **1975**, *201*, 327. [[CrossRef](#)]
- Blumenthal, G.R.; Faber, S.M.; Primack, J.R.; Rees, M.J. Formation of galaxies and large-scale structure with cold dark matter. *Nature* **1984**, *311*, 517. [[CrossRef](#)]
- Davis, M.; Efstathiou, G.; Frenk, C.S.; White, S.D.M. The evolution of large-scale structure in a universe dominated by cold dark matter. *Astrophys. J.* **1985**, *292*, 371. [[CrossRef](#)]
- Komatsu, E.; Smith, K.M.; Dunkley, J.; Bennett, C.L.; Gold, B.; Hinshaw, G.; Jarosik, N.; Larson, D.; Nolte, M.R.; Page, L.; et al. Seven-year Wilkinson Microwave Anisotropy Probe (WMAP) Observations: Cosmological Interpretation. *Astrophys. J. Suppl. Ser.* **2011**, *192*, 18. [[CrossRef](#)]
- Ade, P.A.; Aghanim, N.; Armitage-Caplan, C.; Arnaud, M.; Ashdown, M.; Atrio-Barandela, F.; Aumont, J.; Baccigalupi, C.; Banday, A.J.; Barreiro, R.B.; et al. Planck 2013 results. XVI. Cosmological parameters. *Astron. Astrophys.* **2014**, *571*, A16.
- Milgrom, M. A modification of the Newtonian dynamics as a possible alternative to the hidden mass hypothesis. *Astrophys. J.* **1983**, *270*, 365. [[CrossRef](#)]
- Bekenstein, J.D. Relativistic gravitation theory for the MOND paradigm. *Phys. Rev. D* **2004**, *70*, 083509. [[CrossRef](#)]
- Buchdahl, H.A. Non-linear Lagrangians and cosmological theory. *Mon. Not. R. Astron. Soc.* **1970**, *150*, 1. [[CrossRef](#)]
- Arbey, A. Dark Fluid: A complex scalar field to unify dark energy and dark matter. *Phys. Rev. D* **2006**, *74*, 043516. [[CrossRef](#)]
- Farnes, J.S. A unifying theory of dark energy and dark matter: Negative masses and matter creation within a modified Λ CDM framework. *Astron. Astrophys.* **2018**, *620*, A92. [[CrossRef](#)]
- Clowe, D.; Gonzalez, A.; Markevitch, M. Weak lensing mass reconstruction of the interacting cluster 1E0657-558: Direct evidence for the existence of dark matter. *Astrophys. J.* **2004**, *604*, 596. [[CrossRef](#)]
- Schmidt, F. Weak lensing probes of modified gravity. *Phys. Rev. D* **2008**, *78*, 043002. [[CrossRef](#)]
- Boran, S.; Desai, S.; Kahya, E.O.; Woodard, R.P. GW170817 Falsifies Dark Matter Emulators. *Phys. Rev. D* **2018**, *97*, 041501. [[CrossRef](#)]
- Cheng, H.-C.; Feng, J.L.; Matchev, K.T. Kaluza-Klein Dark Matter. *Phys. Rev. Lett.* **2002**, *89*, 211301. [[CrossRef](#)]
- Oikonomou, V.K.; Vergados, J.D.; Moustakidis, C.C. Direct detection of dark matter rates for various wimps. *Nucl. Phys. B* **2007**, *773*, 19. [[CrossRef](#)]
- Nussinov, S. Technoc cosmology—Could a technibaryon excess provide a “natural” missing mass candidate? *Phys. Lett. B* **1985**, *165*, 55. [[CrossRef](#)]
- Gudnason, S.B.; Kouvaris, C.; Sannino, F. Dark matter from new technicolor theories. *Phys. Rev. D* **2006**, *74*, 095008. [[CrossRef](#)]
- Hubisz, J.; Meade, P. Phenomenology of the littlest Higgs model with T-parity. *Phys. Rev. D* **2005**, *71*, 035016. [[CrossRef](#)]
- Birkedal, A.; Noble, A.; Perelstein, M.; Spray, A. Little Higgs dark matter. *Phys. Rev. D* **2006**, *74*, 035002. [[CrossRef](#)]
- Jungman, G.; Kamionkowski, M.; Griest, K. Supersymmetric dark matter. *Phys. Rep.* **1996**, *267*, 195. [[CrossRef](#)]
- Roszkowski, L.; Sessolo, E.M.; Trojanowski, S. WIMP dark matter candidates and searches—Current status and future prospects. *Prog. Phys.* **2018**, *81*, 066201. [[CrossRef](#)]
- Kortelainen, M.; Kosmas, T.; Suhonen, J.; Toivanen, J. Event rates for CDM detectors from large-scale shell-model calculations. *Phys. Lett. B* **2006**, *632*, 226. [[CrossRef](#)]

26. Toivanen, P.; Kortelainen, M.; Suhonen, J.; Toivanen, J. Large-scale shell-model calculations of elastic and inelastic scattering rates of lightest supersymmetric particles (LSP) on I-127, Xe-129, Xe-131, and Cs-133 nuclei. *Phys. Rev. C* **2009**, *79*, 044302. [[CrossRef](#)]
27. Klos, P.; Menéndez, J.; Gazit, D.; Schwenk, A. Large-scale nuclear structure calculations for spin-dependent WIMP scattering with chiral effective field theory currents. *Phys. Rev. D* **2013**, *88*, 083516. [[CrossRef](#)]
28. Baudis, L.; Kessler, G.; Klos, P.; Lang, R.F.; Menéndez, J.S.; Schwenk, R.A. Signatures of dark matter scattering inelastically off nuclei. *Phys. Rev. D* **2013**, *88*, 115014. [[CrossRef](#)]
29. Vergados, J.D.; Avignone, F.T., III; Pirinen, P.; Srivastava, P.C.; Kortelainen, M.; Suhonen, J. Theoretical direct WIMP detection rates for transitions to the first excited state in Kr-83. *Phys. Rev. D* **2015**, *92*, 015015. [[CrossRef](#)]
30. Vergados, J.D.; Avignone, F.T., III; Kortelainen, M.; Pirinen, P.; Srivastava, P.C.; Suhonen, J.; Thomas, A.W.J. Inelastic WIMP-nucleus scattering to the first excited state in Te-125. *Phys. G: Nucl. Part. Phys.* **2016**, *43*, 115002. [[CrossRef](#)]
31. Pirinen, P.; Srivastava, P.C.; Suhonen, J.; Kortelainen, M. Shell-model study on event rates of lightest supersymmetric particles scattering off Kr-83 and Te-125. *Phys. Rev. D* **2016**, *93*, 095012. [[CrossRef](#)]
32. Pirinen, P.; Kotila, J.; Suhonen, J. Spin-dependent WIMP-nucleus scattering off Te-125, Xe-129, and Xe-131 in the microscopic interacting boson-fermion model. *Nucl. Phys. A* **2019**, *992*, 121624. [[CrossRef](#)]
33. Menéndez, J.; Gazit, D.; Schwenk, A. Spin-dependent WIMP scattering off nuclei. *Phys. Rev. D* **2012**, *86*, 103511. [[CrossRef](#)]
34. Pirinen, P.; Kotila, J.; Suhonen, J. First microscopic evaluation of spin-dependent WIMP-nucleus scattering off W-183. *Phys. Lett. B* **2021**, *816*, 136275. [[CrossRef](#)]
35. Hoferichter, M.; Menéndez, J.; Schwenk, A. Coherent elastic neutrino-nucleus scattering: EFT analysis and nuclear responses. *Phys. Rev. D* **2020**, *102*, 074018. [[CrossRef](#)]
36. Engel, J.; Pittel, S.; Vogel, P. Nuclear physics of dark matter detection. *Int. J. Mod. Phys. E* **1992**, *1*, 1. [[CrossRef](#)]
37. Bernard, V.; Kaiser, N.; Meissner, U.-G. Aspects of chiral pion-nucleon physics. *Nucl. Phys. A* **1997**, *615*, 483. [[CrossRef](#)]
38. Machleidt, R. High-precision, charge-dependent Bonn nucleon-nucleon potential. *Phys. Rev. C* **2001**, *63*, 024001. [[CrossRef](#)]
39. Hjorth-Jensen, M.; Kuo, T.T.S.; Osnes, E. Realistic effective interactions for nuclear systems. *Phys. Rep.* **1995**, *261*, 125. [[CrossRef](#)]
40. Procter, M.G.; Cullen, D.M.; Scholey, C.; Ruotsalainen, P.; Angus, L.; Bäck, T.; Cederwall, B.; Dewald, A.; Fransen, C.; Grahn, T.; et al. Anomalous transition strength in the proton-unbound nucleus I-109. *Phys. Lett. B* **2011**, *704*, 118. [[CrossRef](#)]
41. Bäck, T.; Qi, C.; Moradi, F.G.; Cederwall, B.; Johnson, A.; Liotta, R.; Wyss, R.; Al-Azri, H.; Bloor, D.; Brock, T.; et al. Lifetime measurement of the first excited 2+ state in Te-108. *Phys. Rev. C* **2011**, *84*, 041306. [[CrossRef](#)]
42. Brown, B.A.; Rae, W.D.M. The Shell-Model Code NuShellX@MSU. *Nuc. Data Sheets* **2014**, *120*, 115. [[CrossRef](#)]
43. Shimizu, N.; Mizusaki, T.; Utsuno, Y.; Tsunoda, Y. Thick-restart block Lanczos method for large-scale shell-model calculations. *Comput. Phys. Commun.* **2019**, *244*, 372. [[CrossRef](#)]
44. Symochko, D.M.; Browne, E.; Tuli, J.K. Nuclear Data Sheets for A = 119. *Nucl. Data Sheets* **2009**, *110*, 2945. [[CrossRef](#)]
45. Ohya, S. Nuclear Data Sheets for A = 121. *Nucl. Data Sheets* **2010**, *111*, 1619. [[CrossRef](#)]
46. Ring, P.; Schuck, P. *The Nuclear Many-Body Problem*; Springer: New York, NY, USA, 1980.
47. Vietze, L.; Klos, P.; Menéndez, J.; Haxton, W.C.; Schwenk, A. Nuclear structure aspects of spin-independent WIMP scattering off xenon. *Phys. Rev. D* **2015**, *91*, 043520. [[CrossRef](#)]